# An Initial Study on Frequency and Matching Medium Suitable for Axillary Region Microwave Imaging

*Henrique V. Lopes*, Raquel C. Conceição, and Daniela M. Godinho*

*Abstract* – Microwave imaging (MWI) has been studied as a screening imaging modality for axillary lymph nodes (ALNs) to aid breast cancer staging. The performance of MWI is closely linked to the operating frequency band and the considered matching medium (MM), as these factors ultimately influence image resolution, penetration depth, and contrast. In this preliminary study, the transmission line method is applied to model scenarios capturing anatomic variability in the axillary region. This study aimed to determine an optimal frequency band and MM permittivity range robust to anatomic differences, ensuring effective ALN imaging. The findings underscore the significant impact of anatomic characteristics on electromagnetic signal propagation, identifying a viable frequency band and MM permittivity range applicable across the scenarios considered.

## 1. Introduction

Breast cancer is the second most prevalent cancer worldwide, with more than 2.29 million new cases diagnosed in 2022 [1]. Axillary lymph nodes (ALNs) are usually the first organs to which breast cancer metastases spread, making the evaluation of ALNs crucial for accurate cancer staging and treatment planning [2]. The current evaluation methods of ALNs rely on a combination of imaging techniques and biopsy specimen analysis. Although biopsy procedures remain the gold standard because of their high accuracy, they are invasive, time-consuming, and associated with potential complications, including prolonged recovery and lymphoedema [3]. As a less invasive alternative, imaging techniques, such as ultrasound and magnetic resonance imaging (MRI), are widely employed; however, their sensitivity and specificity vary considerably and often remain suboptimal [4].

Microwave imaging (MWI) has been the focus of significant research for breast cancer screening, offering several potential advantages, including cost-effective hardware, the use of nonionizing radiation, noninvasiveness, and operation at low power levels. Our research group has explored the feasibility of MWI to screen and image level I ALNs, which are the first ALNs to receive drainage from tumor cells. Godinho et al. [5] performed a study on an experimental radar prototype using anatomically realistic phantoms. The system was positioned around the body without physical contact with the body or a matching medium (MM) (i.e., an air-operated prototype) and emitted ultra-wideband (UWB) pulses in the 2GHz to 5 GHz frequency range at −10 dB. Pato et al. [6] evaluated different reconstruction algorithms in a two-dimensional numeric model, featuring a system placed directly on the skin that emitted a Gaussian pulse at a central frequency of 7.5 GHz and a frequency band of 1.56 GHz to 15.36 GHz at −10 dB. In a later study with a different system, Godinho et al. [7] identified a planar 3×3 antenna array in air as the most promising configuration among the tested configurations with nine antennas. This system emitted UWB pulses at a frequency band of 1.3 GHz to 6.7 GHz at −10 dB. These studies resorted to different frequency bands and system configurations, and unlike several breast MWI prototypes, none of these have considered MM. The choice of operating frequency and MM is crucial in MWI system design, as they significantly influence resolution, penetration depth, and contrast, having a direct impact on system performance.

To move toward the design of an optimized system for MWI of the axillary region, this paper aims to analyze the optimal frequency band for MWI of the axillary region across a broad spectrum of anatomic variations. In addition to this, insights into the selection of the MM are given.

## 2. Methodology

To design an MWI system capable of generating an image of the ALNs, the incident power penetrating the ALNs must be maximized, and the spatial resolution must be optimized to detect even small variations within ALNs.

A general and straightforward approach based on the transmission line (TL) formalism, as employed in [8], can be used to establish guidelines for both the optimal frequency band and the range of relative permittivity values for the MM to image the axillary region. In this approach, the interactions between the electromagnetic (EM) wave and the tissues of the axillary region are analyzed using a one-dimensional (1D), multilayer planar model of the target anatomic site, where each tissue is represented by a layer with its natural thickness and dielectric properties. Therefore, in this paper, the TL formalism was applied to a 1D, multilayer planar model of the axillary region for an initial analysis. The target tissues considered here are level I ALNs, which can be located at shallow depths near the skin surface or deeper under the skin [9],

Manuscript received 3 March 2025. This work was supported by the project 3BAtwin (European Union, GA 101159623) and Fundação para a Ciência e Tecnologia UID/00645/2025.

Henrique V. Lopes, Raquel C. Conceição, and Daniela M. Godinho are with the Instituto de Biofísica e Engenharia Biomédica, Faculdade de Ciências, Universidade de Lisboa, 1749-016, Lisbon, Portugal; e-mail: hvlopes@fc.ul.pt, rcconceicao@fc.ul.pt, dmgodinho@fc.ul.pt.

Table 1. Models of the axillary region

| Models | Skin | Adipose | Muscle | ALN |
|---|---|---|---|---|
| M1 | 2 | 60 | 0 | Inf |
| M2 | 1.2 | 0.8 | 0 | Inf |
| M3 | 2 | 10 | 0 | Inf |
| M4 | 2 | 30 | 0 | Inf |
| M5 | 2 | 30 | 8 | Inf |

The thickness of each tissue is indicated in millimeters (mm).

with varying thicknesses of the overlying tissues (i.e., skin and adipose tissue). Although these ALNs are typically more superficial and not surrounded by muscle, muscle may be detected due to inter-individual anatomic variability or suboptimal orientation of the antenna array. Consequently, this study considered five models of the axillary region (Table 1) with varying tissue layer thicknesses, including a case where muscle tissue is present between the antenna and the ALNs.

The thicknesses of each tissue layer were extracted from experimental studies [9–12], and the target region (ALN) was modelled as a half-space (i.e., homogeneous, semi-infinite medium).

To use the TL formalism, each tissue layer is associated with a characteristic impedance, as shown in Figure 1. The characteristic impedance of the $n^{th}$ tissue layer is given by:

$$Z_n = \sqrt{\frac{\mu_0}{\varepsilon_0 \varepsilon_n}} \tag{1}$$

where $\mu_0$ and $\varepsilon_0$ denote the magnetic permeability and relative permittivity of free space, respectively, and $\varepsilon_n$ denotes the complex permittivity of the tissue layer under consideration. The tissues' dispersive behavior was modelled by the Debye model, as shown in Figure 2, where the values were set according to [13, 14] and reported in Table 2. To evaluate the propagation of the EM wave in the considered biological tissues, the penetration depth of the signal, as a function of frequency, is shown in Figure 3.

The amount of incident power that penetrates into the ALNs was quantified by the transmission coefficient ($T$), which is defined as:

$$T = 1 - |\Gamma| \tag{2}$$

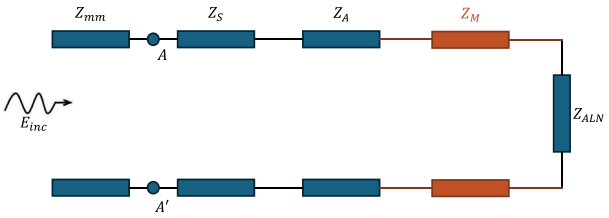


Figure 1. The transmission line model of 1D axillary region. $Z_{mm}$, $Z_S$, $Z_A$, $Z_M$, and $Z_{ALN}$ represent the impedance of MM, skin, adipose tissue, muscle, and axillary lymph node, respectively. In models where muscle is not considered, the respective impedance (in orange) is removed.

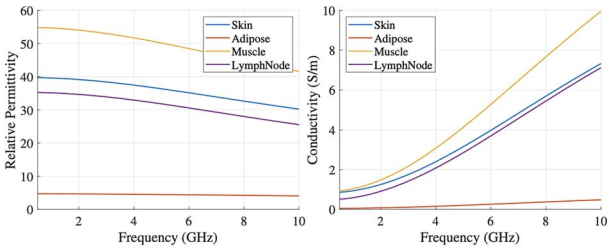


(a) Relative permittivity. (b) Conductivity.

Figure 2. Dielectric properties of the tissues considered in the axillary region models.

where $\Gamma$ is the reflection coefficient at section $AA'$, corresponding to the interface between the MM and the skin, and is given by:

$$\Gamma = \frac{Z_{AA'} - Z_{mm}}{Z_{AA'} + Z_{mm}} \tag{3}$$

Here, $Z_{mm}$ denotes the characteristic impedance of the matching medium, while $Z_{AA'}$ represents the characteristic impedance of the axilla. Based on these tissue properties and considering the operating frequency $f$ within the range of 0.5 GHz to 10 GHz, $Z_{AA'}$ is determined by solving the equivalent TL problem, that is, iteratively solving the following equation:

$$Z_{Total} = Z_n \frac{Z_{Total-1} + jZ_n \tan(k_n \times d_n)}{Z_n + jZ_{Total-1} \tan(k_n \times d_n)} \tag{4}$$

where $k_n = \frac{\omega}{c\sqrt{\varepsilon_n(f)}}$ is the wave number in the $n^{th}$ tissue layer, with ω denoting the angular frequency, and $d_n$ representing the thickness of the $n^{th}$ tissue layer.

Furthermore, $T$ was evaluated not only as a function of frequency but also as a function of the relative permittivity of a lossless MM, varying within the range of 1 to 80, to determine a feasible range for the relative permittivity of the MM.

The results obtained with the TL modelling of the 1D multilayered model were validated with an MRI-derived anthropomorphic model [13]. A synthetic ALN was introduced to this model to allow full control over its positioning [15]. Three-dimensional finite difference time-domain simulations were performed with an antenna array composed of 12 monostatic Hertzian dipole antennas, arranged in a 3×4 grid on the skin surface. The UWB radar images were reconstructed using the delay-and-sum algorithm [16].

Table 2. Debye model parameters for skin, adipose tissue, muscle, and healthy ALNs (valid from 1–20 GHz) [13, 14]

| | Skin | Adipose | Muscle | ALN |
|---|---|---|---|---|
| $\varepsilon_\infty$ | 15.93 | 3.12 | 21.66 | 10.94 |
| $\sigma_s(S/m)$ | 0.83 | 0.05 | 0.89 | 0.48 |
| $\Delta\varepsilon$ | 23.83 | 1.59 | 33.24 | 24.35 |
| $\tau(ps)$ | 13.00 | 13.00 | 13.00 | 13.00 |

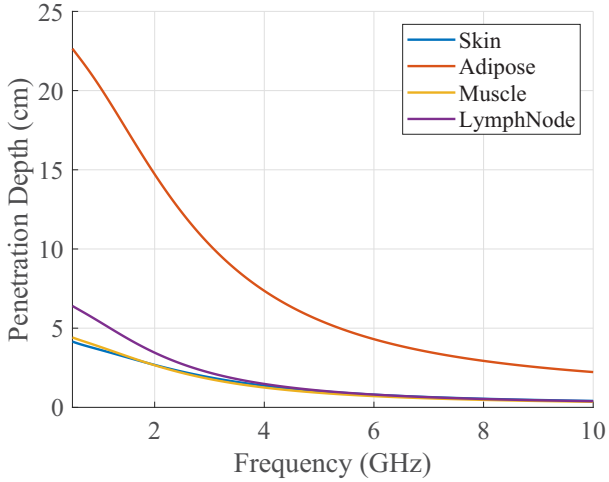


Figure 3. Penetration depth of the considered tissues in the axillary region.

## 3. Results and Discussion

Figure 4 shows the imaging results for each model under analysis. M1 and M2 represent two extreme cases, with the ALN positioned at the greatest depth and the most superficial depth, respectively. M3 and M4 correspond to intermediate models, while M5 includes a muscle layer of 8 mm between the adipose tissue and the ALN.

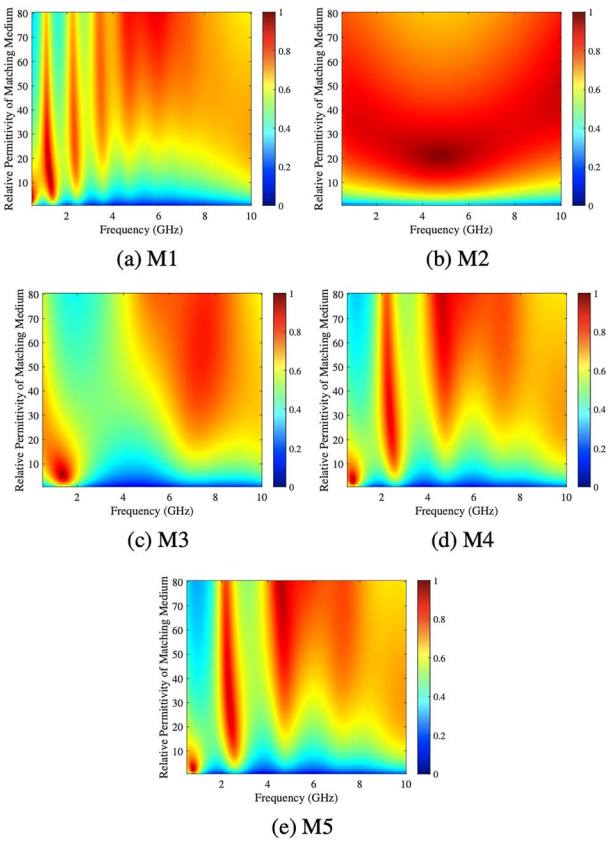


Figure 4. Transmission coefficient plots for each model under analysis (M1-M5). The transmission coefficient is shown as a function of frequency and relative permittivity of the MM. Warmer colors represent higher transmission coefficients.

Table 3. Summary of the optimal frequency bands and relative permittivity value for the MM for the models under analysis, considering transmission coefficient values higher than 0.53.

| Models | Frequency band, GHz | Relative permittivity of MM |
|---|---|---|
| M1 | 0.5–2.6 | 13–23 |
| M2 | 0.5–10 | 9–80 |
| M3 | 0.5–2.3 | 9–20 |
| M4 | 0.5–3.0 or 2.0–4.6 | 15–19 or 31–69 |
| M5 | 2.0–3.16 | 15–73 |

This analysis aims to identify regions in each plot where the transmission coefficient is higher (i.e., warmer colors), indicating that greater incident power reached the ALNs, while ensuring that the EM signal reaches the ALNs by analyzing the penetration depth in each biological tissue within the selected frequency range. Furthermore, to guarantee a feasible spatial resolution for radar imaging, the minimum bandwidth of the selected frequency range was set to approximately 2 GHz.

Our current prototype employs a radar-based system with a monostatic configuration, requiring the EM signal to travel from the antenna to the target (ALN) and back. For instance, in model M1, the signal must penetrate 12 cm of adipose tissue and 0.4 cm of skin. Of note, the penetration depth in adipose tissue falls below 12 cm for frequencies above 2.57 GHz. In contrast, the penetration depth in skin remains above 0.4 cm across the considered frequency range, as is shown in Figure 3.

Tables 3 and 4 show the optimal frequency band for each model, along with the range of relative permittivity for the MM that ensures minimum transmission coefficient values of 0.53 and 0.47, respectively.

The results indicate that the optimal frequency band for imaging the axillary region lies between 0.5 GHz and 2.3 GHz (with a bandwidth of 1.8 GHz), with a MM relative permittivity between 15 and 19. This frequency band ensures high transmission coefficients across all analyzed models, maximizing power delivery to the target. Additionally, it provides the greatest penetration depth through the considered tissues. However, the presence of a muscle layer poses challenges, such scenarios are not typically observed when imaging level I ALNs. Nonetheless, with an 8 mm muscle layer, sufficient signal power transmission to the ALN within this frequency band is achievable.

Table 4. Summary of the optimal frequency bands and relative permittivity value for the MM for the models under analysis, considering transmission coefficient values higher than 0.47.

| Models | Frequency band, GHz | Relative permittivity of MM |
|---|---|---|
| M1 | 0.5–3.0 | 13–23 |
| M2 | 0.5–10 | 9–80 |
| M3 | 0.5–3.0 | 17–30 |
| M4 | 0.5–3.0 or 2.0–4.6 | 10–24 or 31–69 |
| M5 | 0.5–3.0 | 13–20 |

If a broader frequency band is required, the range from 0.5 GHz to 3.0 GHz, with an MM relative permittivity between 17 and 23, may be selected, though it includes a low transmission coefficient of 0.47. This broader band introduces greater signal attenuation, potentially affecting the quality of the reconstructed images. Therefore, our study indicates that the choice between these frequency ranges (0.5–2.3 GHz or 0.5–3.0 GHz) should be considered in the imaging system's design parameters and the acceptable signal attenuation threshold for the intended application.

This approach enabled an initial feasibility study of imaging the axillary region for ALN detection by facilitating the optimization of both the relative permittivity of MM and the frequency band. Although the TL model offers a convenient analytical method to assess wave propagation in a 1D multilayered structure, it has important limitations that must be recognized. First, the model oversimplifies the anatomic complexity of the axillary region by representing the ALN as a 1D layer embedded within fat, neglecting its realistic geometry as a compact, localized target. This abstraction disregards wave propagation effects associated with small curved interfaces. Second, the TL approach assumes idealized plane-wave propagation at normal incidence, which fails to capture the influence of the near-field radiation pattern of the antenna on energy delivery. Last, the maximization of the incident power penetrating the ALN does not necessarily imply successful image reconstruction or target detectability. Image quality depends on spatial resolution, contrast, and the ability to handle multiple reflections.

Therefore, the TL results were validated with an anthropomorphic model. Three scenarios were simulated to evaluate the influence of MM and operating frequency, based on the optimal and suboptimal conditions predicted by the TL analysis. The scenarios were as follows: (1) the optimal scenario used a modulated Gaussian pulse centered at 1.7 GHz (–10 dB bandwidth: 0.68–2.66 GHz) with an MM defined by $\varepsilon_\infty = 17$, $\Delta\varepsilon = 2$, $\sigma_s = 0.005$ S/m, and $\tau = 13$ ps; (2) a suboptimal scenario with a pulse centered at 1.7 GHz (–10 dB bandwidth: 0.68–2.66 GHz) and an MM with $\varepsilon_\infty = 1$, $\Delta\varepsilon = 2$, $\sigma_s = 0.01$ S/m, and $\tau = 13$ ps; (3) a second suboptimal scenario with a pulse centered at 8.5 GHz (–10 dB bandwidth: 7.44–9.56 GHz) and an MM with $\varepsilon_\infty = 17$, $\Delta\varepsilon = 2$, $\sigma_s = 0.005$ S/m, and $\tau = 13$ ps.

Figure 5 presents the reconstructed images for the three scenarios. The upper right and bottom left images illustrate the effect of the MM on image quality, with superior results obtained using the optimal MM. Similarly, a comparison between the upper right and bottom right images highlights the improvement in image quality when the operating frequency lies within the identified optimal frequency band. While multiple factors influence image reconstruction in realistic scenarios, these results support the validity of the TL predictions, particularly regarding the selection of frequency and the relative permittivity of the MM.

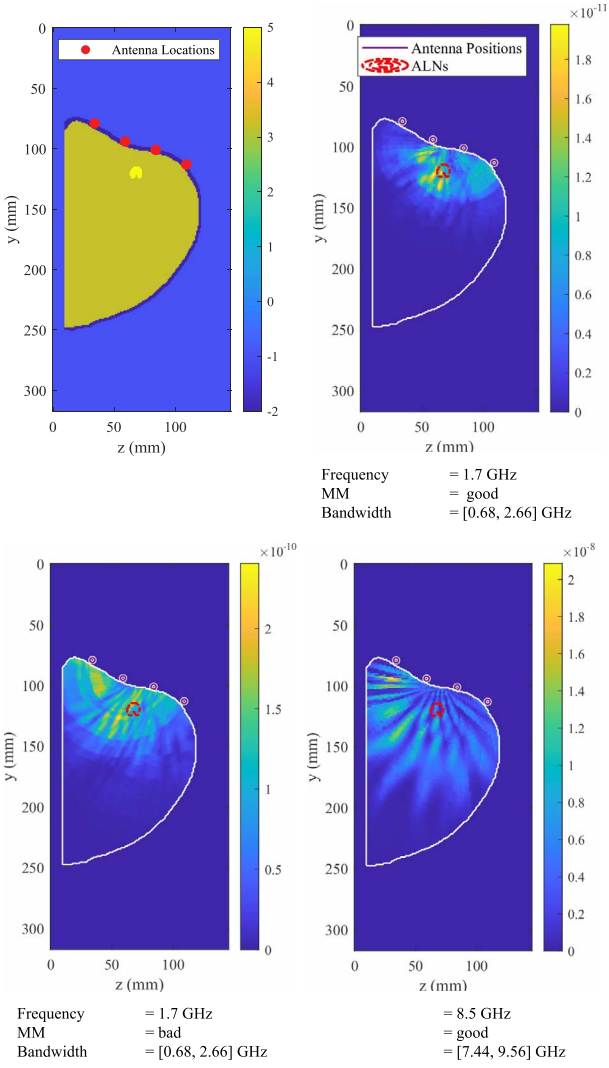


Figure 5. Axial view of the anthropomorphic axilla model (top left) and reconstructed images using the Delay-and-Sum algorithm from full-wave simulation data under three scenarios (top right, bottom left, bottom right). The good matching medium (MM) is defined by $\varepsilon_\infty = 17$, $\Delta\varepsilon = 2$, and $\sigma_s = 0.005$ S/m; the bad by $\varepsilon_\infty = 1$, $\Delta\varepsilon = 2$, $\sigma_s = 0.01$ S/m, and with $\tau = 13$ ps.

## 4. Conclusions and Future Work

This study aimed to identify the optimal frequency band for MWI of the axillary region and determine the most suitable MM. This was achieved by employing 1D models of the axilla within a TL framework—an approach that provides useful information on wave propagation characteristics despite not being an imaging solution. Body models representing extreme scenarios, such as shallow and deep ALNs and the inclusion of muscle tissue, were considered. The results suggest that the optimal frequency band for imaging the axillary region lies between 0.5 GHz and 2.3 GHz, with an MM relative permittivity range of 15 to 19. This frequency band ensures high transmission coefficients across all analyzed models, maximizing power delivery to the target. The above values

derived from the proposed simplified 1D approach were applied in full-wave simulations incorporating a realistic anthropomorphic model of the axilla. The findings showed improved image quality.

Future work will focus on validating the identified frequency band and range of relative permittivity values using more anthropomorphic models of the axillary region, including metastatic axillary models [13].

## 5. References


1. The Global Cancer Observatory – World Health Organization, "Breast cancer fact sheets," http://gco.iarc.fr/today (Accessed on 03/02/2025).
2. G. H. Lyman, A. E. Giuliano, M. R. Somerfield, A. B. Benson III, D. C. Bodurka, et al., "American Society of Clinical Oncology guideline recommendations for sentinel lymph node biopsy in early-stage breast cancer," *Journal of Clinical Oncology*, **23**, 30, October 2005, pp. 7703-7720.
3. G. H. Lyman, M. R. Somerfield, L. D. Bosserman, C. L. Perkins, D. L. Weaver, et al., "Sentinel Lymph Node Biopsy for Patients With Early-Stage Breast Cancer: American Society of Clinical Oncology Clinical Practice Guideline Update," *Journal of Clinical Oncology*, **35**, 5, February 2017, pp. 561-564.
4. H. Rahbar, S. C. Partridge, S. H. Javid, and C. D. Lehman, "Imaging Axillary Lymph Nodes in Patients With Newly Diagnosed Breast Cancer," *Current Problems in Diagnostic Radiology*, **41**, 5, September-October 2012, pp. 149-158.
5. D. M. Godinho, J. M. Felício, C. A. Fernandes, and R. C. Conceição, "Experimental Evaluation of an Axillary Microwave Imaging System to Aid Breast Cancer Staging," *IEEE Journal of Electromagnetics, RF and Microwaves in Medicine and Biology*, **6**, 1, 2022, pp. 68-76.
6. M. Pato, R. Eleutério, R. C. Conceição, and D. M. Godinho, "Evaluating the Performance of Algorithms in Axillary Microwave Imaging Towards Improved Breast Cancer Staging," *Sensors*, **23**, 3, 2023, p. 1496.
7. D. M. Godinho, P. L. Cidadão, and R. C. Conceição, "Impact of Antenna Configuration and Artefact Removal Algorithms for Axillary Microwave Imaging," 2024 4th URSI Atlantic Radio Science Meeting (AT-RASC), Meloneras, Spain, May 19–24, 2024, pp. 1-3.
8. R. Scapaticci, L. Di Donato, I. Catapano, and L. Crocco, "A Feasibility Study on Microwave Imaging for Brain Stroke Monitoring," *Progress In Electromagnetics Research B*, **40**, May 2012, pp. 305-324.
9. D. M. Godinho, C. Silva, C. Baleia, J. M. Felicio, T. Castela, et al., "Modelling Level I Axillary Lymph Nodes depth for Microwave Imaging," *Physica Medica*, **104**, December 2022, pp. 160-166.
10. A. Chanda and G. Singh, "Skin," in: A. Chanda and G. Singh, (eds.), *Mechanical Properties of Human Tissues*, Singapore, Springer Nature, 2023, pp. 13-23.
11. E. W. S. Soares, "Anatomical Variations of the Aaxilla," *SpringerPlus*, **3**, 1, June 2014, p. 306.
12. A. F. Bueno, F. d. A. Lemos, M. E. Ferrareze, W. A. M. d. Santos, F. V. Veronese, et al," Muscle Thickness of the Pectoralis Major and Rectus Abdominis and Level of Physical Activity in Chronic Hemodialysis Patients," *Brazilian Journal of Nephrology*, **39**, 4, October-December 2017, pp. 391-397.
13. D. M. Godinho, J. M. Felicio, T. Castela, N. A. Silva, M. de Lurdes Orvalho, et al., "Development of MRI-Based Axillary Numerical Models and Estimation of Axillary Lymph Node Dielectric Properties for Microwave Imaging," *Medical Physics*, **48**, 10, 2021, pp. 5974-5990.
14. S. Gabriel, R. W. Lau, and C. Gabriel, "The Dielectric Properties of Biological Tissues: III. Parametric Models for the Dielectric Spectrum of Tissues," *Physics in Medicine & Biology*, **41**, 11, 1996, p. 2271.
15. D. M. Godinho, *Microwave Imaging to Improve Breast Cancer Diagnosis*, Ph.D. thesis, Faculdade de Ciências da Universidade de Lisboa, Portugal, 2022.
16. S.C. Hagness, A. Taflove, and J. Bridges, "Two-Dimensional FDTD Analysis of a Pulsed Microwave Confocal System for Breast Cancer Detection: Fixed-Focus and Antenna-Array Sensors," *IEEE Transactions on Biomedical Engineering*, **45**, 12, December 1998, pp. 1470-1479.